Compressive Behavior and Nonlinear Load Carrying Capacity of Multiple-Shape Concrete Filled Double-Skin Steel Tubular Columns

Fayaz A. Sofi [iD] **, Mohammad Rafiq Joo** [iD] **, R. Seetharaman, and Mohammad Zakir**

1 Introduction

Concrete filled double-skin steel tubular (CFDST) columns with steel inner and outer tubes belong to a category of modern composite columns in which concrete is filled in the space between the two tubes. CFDST columns are optimized to offer benefits and advantages similar to steel–concrete composite construction by taking advantage of strengths of both concrete and steel. The steel tubes act as longitudinal reinforcement and permanent formwork in these columns and also provide potential confinement for enhancing the structural behavior of the concrete infill. The composite action of steel and concrete leads to improved structural characteristics, including potential higher axial-load capacity and ductility, reduced self-weight and cost, better fire resistance and seismic behavior, cost, and space efficiency compared to conventional steel or reinforced concrete columns. CFDST columns find potential applications in onshore and offshore structures to increase buoyancy, medium and high-rise structures, bridge piers, large span buildings for extreme dynamic, and fire loading scenarios [1–4]. The outer and inner tubes can be provided with multiple cross-sectional shapes such as circular (C) or square (S) tubes. Thus, resulting in multiple configurations of cross sections shown in Fig. 1 such as outer-circle and inner-circle (CC), outer-circle and inner-square (CS), outer-square and inner-circle (SC), and outer square and inner-square (SS).

Each of these column cross-sectional shapes is expected to result in different axial load compression behavior and ultimate load carrying capacity because of varying degree of concrete confinement provided by outer and inner tubes [5, 6]. Different experimental research studies [7–17] investigated behavior of CFDST columns under axial compression. These research studies focused on individual

F. A. Sofi (✉) · M. R. Joo · R. Seetharaman · M. Zakir
National Institute of Technology Srinagar, Jammu and Kashmir 190006, India
e-mail: sofifayaz@nitsri.ac.in
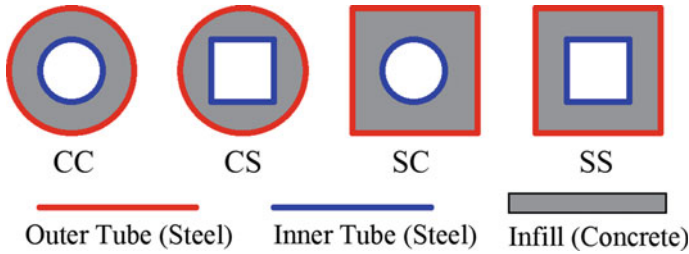
Fig. 1 CFDST column cross sections; CC = circle-circle; CS = circle-square; SC = square-circle; SS = square-square

cross-sectional shapes to study behavior of CFDST columns under axial compressive loading. Other studies [18–27] validated experimentally observed behavior of CFDST columns using finite element (FE) modeling, and extended studies through parametric studies using validated numerical models for each of the individual cross-sectional shapes. In these research efforts, it is established that increase in material strengths (either of steel tubes or concrete infill) or geometric characteristics (such as thickness of steel tubes or ratio of steel to concrete area in a cross section) enhances column axial load capacity. Whereas, other factors such as slenderness ratios of steel tubes and ratio of inner-to-outer tube diameters have negative influence on CFDST column axial load capacity. The comparative behavior of the CFDST columns with multiple shapes and having equivalent cross-sectional area is not yet available in the present literature.The relative influence of inner and outer tube shapes on the confined concrete behavior is scantly investigated either experimentally or analytically. The outer tube is majorly providing confinement for the sandwiched concrete resulting in enhanced performance than the inner steel tube [1]. The cross-sectional shape of the outer tube can result in varying confinement in the concrete core in the cross section. Such as in SS shape CFDST column, the confinement to concrete is expected to vary from mid-flat sides from a minimum to the maximum at corners compared to more uniform case in a CC shape. Such nonuniform confinements in SS shaped cross section can trigger mid-flat side bucking of the inner steel tube toward the inner void compared to absent or reduced local buckling of CC shapes. Thus, study of comparative behavior of CFDST columns of multiple cross-sectional shapes needs to be investigated to compare their relative structural performances when different shapes are provided with equivalent cross-sectional areas.

The previous research studies, both experimental and numerical, were limited to behavior of CFDST columns with individual cross-sectional shapes. General guidance regarding influence of cross-sectional shape on compressive behavior and nonlinear load carrying capacity of CFDST columns is scant in existing literature and standard design specifications such as International Building Code. To the authors' knowledge, no major comparative study on the performance of multiple-shapes of CFDST columns has been carried out to investigate and compare their relative performance when all shapes are provided with equivalent cross-sectional areas. The present study builds on the previous research efforts with an objective to perform

comparative study on the axial compression behavior of CFDST columns of multiple cross-sectional shapes (recall Fig. 1). The influence on ultimate load carrying capacity was investigated using nonlinear finite element analysis (NLFEA) for four different cross-sectional shapes (i.e., CC, CS, SC, and SS). For this parametric study, all the column shapes were provided with same equivalent cross-sectional areas of inner and outer steel tubes and concrete infill. The accuracy and reliability of nonlinear FE models were first validated against experimental results of 40-documented CFDST column tests (16 specimens for CC and 8 each from CS, SC, and SS shapes) available in existing literature.

2 Finite Element Modeling

The finite element (FE) analysis approach was used in the present study to generate analytical 3D-models of CFDST columns in ANSYS 19.0 [28]. The selection of elements, simulation of boundary conditions and load application, and idealization of contact interfaces between different material interfaces was automated and executed using ANSYS parametric design language (APDL), similar to research studies [29–32]. Thus, a customized FE modeling framework was developed using APDL for generation of numerical models incorporating structural and geometrical characteristics such as mapped meshing in cross sections, interaction between different structural components, constitutive material modeling, boundary conditions, and load application (Fig. 2). Different cross-sectional shapes (i.e., CC, CS, SC, and SS) considered in this study were provided with mapped meshing across the column components (Fig. 2a). Inner and outer steel tubes and end loading plates were idealized with 4-node shell elements (SHELL181) and concrete infill was simulated using 8-node solid elements (SOLID185). The individual meshed column components are shown in Fig. 2b. The interaction between steel tubes and concrete infill both on inner and outer surfaces was modeled with 2-node rigid beam elements, i.e., kinematic multi-point constraints (MPC184) simulated by zero length elements. Rigid beam MPCs related the shell element rotations for outer and inner tubes to the solid element translations in the concrete core at the concrete-steel interface. The rigid beams thus generated kinematic constraint equations for relating translational DOFs from solid elements to shell element rotational DOFs at the hybrid material interface. The analysis results from MPC interface modeling were compared to using nonlinear contacts, and the analysis results showed insignificant difference. However, the advantage of using rigid beam MPCs stabilized the analysis by avoiding generation of nonlinear contact definition forces at the interface in the numerical models and was thus adopted in this study.

Surface-to-surface 4-node contact (CONTA173) and target elements (TARGE170) simulated interaction of steel end plates with concrete infill in the cross section. Steel end plates were set as contact surface and concrete infill in the column end cross sections as target for surface-to-surface contacts. The interaction between inner and outer steel tubes with column end plates was idealized
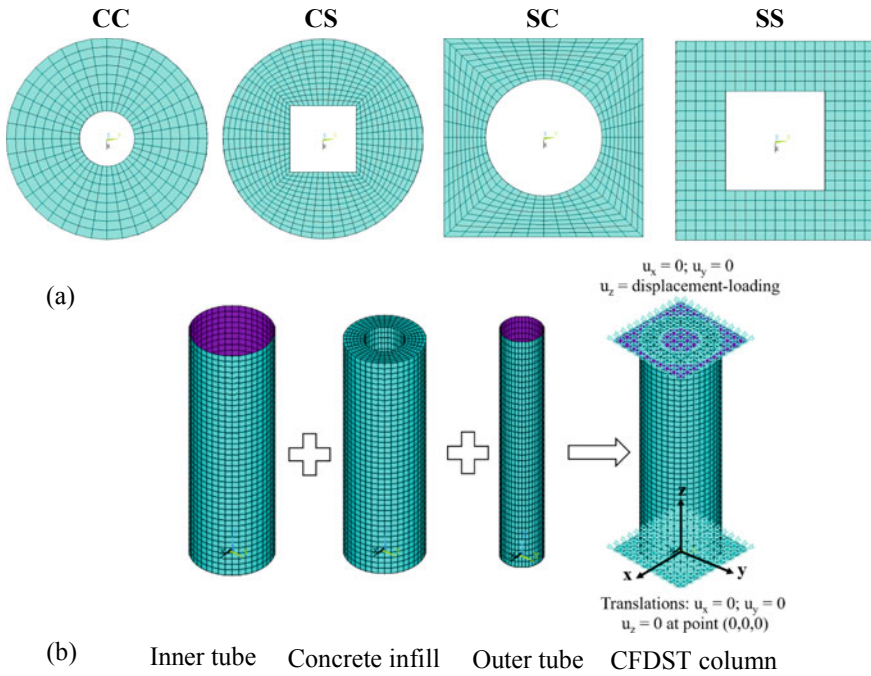
Fig. 2 Finite element modeling: **a** meshing in cross sections; **b** assembled components of CFDST columns; CC = circle-circle; CS = circle-square; SC = square-circle; SS = square-square

by node-to-surface contacts. The edge nodes of steel tubes were set as contact nodes using single node elements (CONTA171) and the column end plates as target surface similar to previously simulated surface-surface contact definition.

FE mesh sizes in the column cross section and in longitudinal direction were seen sensitive to analysis results. Element size of less than 15 mm in cross section and 20 mm in the longitudinal directions was sufficient for obtaining consistently converged results with desired accuracy in terms of axial load–displacement curves. Meshes in the end plates were made slightly coarse with an element size of 15–20 mm for their simulated linear-elastic response.

The boundary conditions have significant influence on column behavior and its load carrying capacities. In this study, all the numerical models were provided with simply supported boundary conditions. The end-plate nodes on both the top and bottom sides of the column were restrained against translations in the plane of cross section, i.e., x- and y-global coordinate directions. Whereas, the translation along the longitudinal direction of column, i.e., z-direction was restrained only for bottom end plate at a single node nearest to the centroid of the column. The top-end plate was free to move in z-coordinate direction. The axial compression was simulated using z-direction prescribed displacement loading of top-end plate. All nodes of the top steel plate were given a displacement along the longitudinal direction of the column

equal to 1/6th of the column height. The details of constitutive material modeling are discussed in the following subsections.

2.1 Constitutive Material Modeling

There are two different materials used in CFDST columns, i.e., steel and concrete. Extensive research studies are available in literature for constitutive material models, particularly for simulating behavior of confined concrete in between the two steel tubes. In this study, concrete material plasticity was idealized with multilinear kinematic hardening rule using microplane failure theory [33] in which uniaxial stress–strain curves of concrete are applied on each microplane. Kinematic hardening rule for plastic flow in concrete material was followed considering the expected decreasing trend of the post-peak axial load–deflection behavior, similar to experimentally observed results used for validation of numerical models. At macroscopic level, strain tensors are kinematically related to their microplane counterparts. The steel components used an isotropic-hardening plasticity rule with Von Mises yield criteria. A brief summary of the constitute material models used in this study for concrete and steel based on literature is provided here.
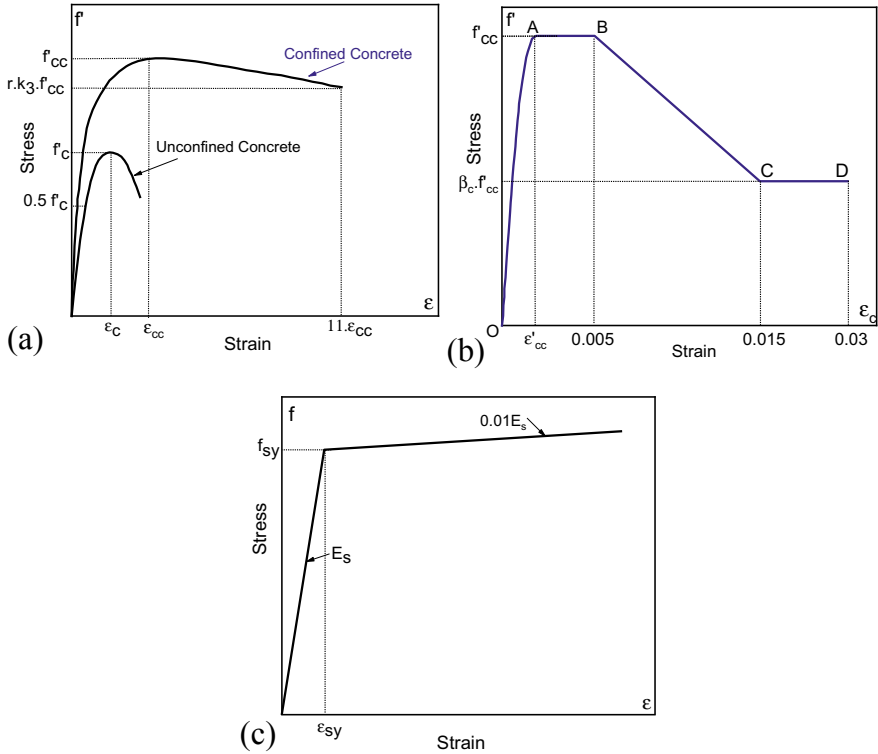
2.1.1 Concrete

In this study, two different nonlinear stress–strain models for confined concrete shown in Fig. 3a, b were used for concrete infill to capture its varying degrees of confinement level depending on DSTC column cross-section shape. Confined stress–strain curve given in study [20] was used in CC and CS numerical models and is referred hereafter as Pagoulatou model. Whereas, stress–strain curve for confined concrete from research study [34] was used in SS shape and is referred as Zhao model in this paper. For columns with SC shape, a modified version of Zhao model incorporating modifications from study [21] was used to simulate concrete confinement behavior. The salient features of each of these concrete stress–strain curves are briefly discussed here.

Figure 3a shows the unconfined and confined stress–strain curves for concrete. Based on Pagoulatou model, peak confined stress (f'_{cc}) and corresponding confined strain (ε_{cc}) can be obtained by Eqs. 1 and 2 using lateral confinement factor (f_1) provided elsewhere [20].

$$f'_{cc} = f'_c + k_1 f_1 (\text{MPa}) \tag{1}$$

$$\varepsilon_{cc} = \varepsilon_c \left(1 + k_2 \frac{f_1}{f'_c}\right) \tag{2}$$

Fig. 3 Material stress–strain curves: **a** concrete for CC and CS; **b** concrete for SC and SS; **c** steel tubes; CC = circle-circle; CS = circle-square; SC = square-circle; SS = square-square

where $k_1 = 4.1$ and $k_2 = 20.5$ are fixed constants and f_c' is unconfined cylinder strength corresponding to strain $\varepsilon_c = 0.003$. Accordingly, confined stress (f') at any strain (ε) was obtained by Eq. 3 from study [20].

$$f' = \frac{E_{cc}\varepsilon}{1 + (R + R_E - 2)\left(\frac{\varepsilon}{\varepsilon_{cc}}\right) - (2R - 1)\left(\frac{\varepsilon}{\varepsilon_{cc}}\right)^2 + R\left(\frac{\varepsilon}{\varepsilon_{cc}}\right)^3}(\text{MPa}) \qquad (3)$$

where E_{cc} is modulus of elasticity for confined concrete given in Eq. 4 [35]. The parameters R_E, R, k_3, and r needed for obtaining descending portion of confined stress–strain curve in Fig. 3a were obtained from literature [20].

$$E_{cc} = 4700\sqrt{f_{cc}'}(\text{MPa}) \qquad (4)$$

In Zhao model, the confined stress (f') at any strain (ε) was obtained by Eq. 5, which was originally proposed by Popovics [36] and later modified by Mander et al. [37], to simulate stress–strain behavior of SS columns [34].

$$f' = \frac{f'_{cc}\left(\frac{\varepsilon}{\varepsilon_{cc}}\right)r_m}{r_m - 1 + \left(\frac{\varepsilon}{\varepsilon_{cc}}\right)^{r_m}} \tag{5}$$

where the details of obtaining peak confined stress (f'_{cc}) at strain (ε_{cc}) along with all relevant parameters are given elsewhere [34].

The modified version of Zhao model given in study [21] and shown in Fig. 3b was used to simulate confined concrete behavior in SC columns. This stress–strain curve consists of four segments such as OA, AB, BC, and CD. First segment OA of the concrete curve was evaluated as given in research study [37]. The portions AB, BC, and CD of the stress–strain curve were modeled as per recommendations from the literature [38], where β_c factor in Fig. 3b reflects confinement effect on concrete ductility.

2.1.2 Steel

Steel stress–strain curve was simulated by typical elasto-plastic curve shown in Fig. 3c, similar to study [39]. The stress (f) at any strain (ε) in the linear-elastic and nonlinear plastic segments of this curve can easily be evaluate by Eqs. (6) and (7), respectively.

$$f = E_s \times \varepsilon \text{ for } \varepsilon \leq \varepsilon_{sy} \tag{6}$$

$$f = f_{sy} + 0.01E_s \times \left[\varepsilon - \varepsilon_{sy}\right] \text{ for } \varepsilon > \varepsilon_{sy} \tag{7}$$

where f_{sy} = yield stress at strain (ε_{sy}). The modulus of elasticity (E_s) and poisson's ratio (ν_s) of 200 GPa and 0.3, respectively, was used in FE analysis in this study.

3 Results and Discussions

In this study, 80 CFDST column models provided with four different cross-sectional shapes (i.e., CC, CS, SC, and SS) were analyzed using NLFEA. Among these, 40 nonlinear FE analyses (i.e., 16 in CC and 8 each of CS, SC, and SS column shapes) were performed on experimentally tested specimens, having available results, geometry, and material characteristics in documented literature [8, 9, 11–13]. Additionally, 40 numerical models with 10 columns for each of CC, CS, SC, and SS shapes were created, such that each of these columns were provided with equivalent cross-sectional areas for each inner tube, outer tube, and concrete infill. The results of these nonlinear FE analyzes are discussed in the subsections below.

3.1 Validation of Numerical Models

Figure 4 shows a comparison of experimental and analytical curves for axial load vs deflection and axial load vs strain results of representative column samples in each considered cross-sectional shape category. Other details, such as location of deflection and strain measurements, material properties and geometric characteristics in analytical study exactly concur with the actual documented experimental studies [8, 9, 11–13]. Figure 4a–d, respectively, for CC, CS, SC, and SS shows that adopted NLFEA can capture CFDST column behavior satisfactorily, including nonlinear pre-peak and post-peak curves. The CFDST columns depicted ductile behavior during experiments, which was satisfactorily captured in analytical models for all shapes. This validation study further verified that the degree of concrete confinements was captured correctly by using Pagoulatou material model for CC and CS column shapes and similarly Zhao model in SS column. However, modified Zhao material model used in SC columns resulted in stiffer post-peak behavior compared to experimental results (Fig. 4c). This disparity in post-peak axial load–deflection behavior of SC shaped CFDST columns can be attributed to the fact that the material model used
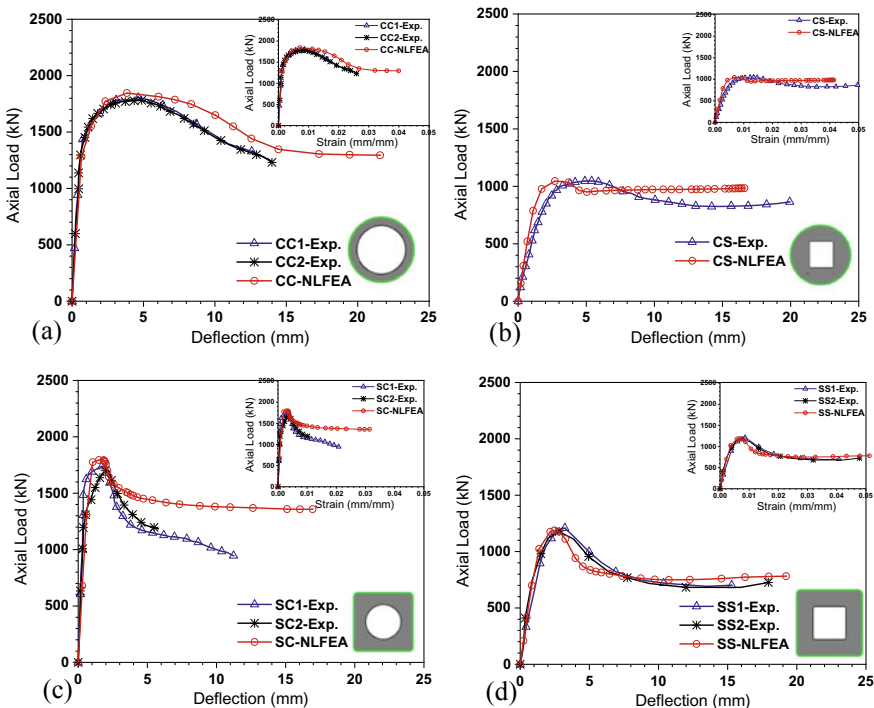
Fig. 4 Axial load–deflection / strain characteristics of CFDST columns, experimental vs analytical results: **a** circle-circle (CC); **b** circle-square (CS); **c** square-circle (SC); **d** square-square (SS)

Table 1 Comparison of experimental and analytical axial load capacities for typical CFDST columns

Column label	Ultimate axial load capacity		$\frac{P_{ult, NLFEA}}{P_{ult, Exp}}$
	$P_{ult, Exp.}$ (kN)	$P_{ult, NLFEA}$ (kN)	
CC1[a]	1790	1818	1.02
CC2[a]	1791		1.02
CS	1050	1074	1.02
SC1[a]	1725	1789	1.04
SC2[a]	1710		1.05
SS1[a]	1194	1189	1.00
SS2[a]	1210		0.98

in FE analysis for SC shape in the present study was originally developed by Zhao et al. [34] for SS cross-sectional shape. The modified Zhao material model used in the present paper was used for analytical modeling in SC shapes similar to other studies [21], wherein the difference in the axial load–deflection post-peak behavior was similarly reported.

Table 1 summarizes the experimental and analytical ultimate axial load capacities of the columns shown in Fig. 4. It can be seen that NLFEA predicted axial load carrying capacities of CFDST columns in all considered shapes within 1–5% maximum error compared to experimentally evaluated results. The average ratios of axial load capacities evaluated using NLFEA to experimental results ($P_{NLFEA}/P_{Exp.}$) on all 40 experimentally tested columns were: 0.98 for CC, 1.05 for CS, 0.99 for SC, and 1.03 for SS. This validation study provided the confidence that adopted NLFEA procedures can be further extended to study influence of column cross-sectional shape on resulting concrete infill confinement and ultimate axial load capacities of CFDST columns.

3.2 Results of Parametric Study

In this section, the results of NLFEA on additional 40 numerical models depict the influence of column cross-sectional shape on concrete infill confinement and ultimate axial load capacity. Each of 10-sets of numerical models were generated, such that columns across a typical set had same cross-section area of inner tube, outer tube, and concrete infill for four column shapes, i.e., CC, CS, SC, and SS. All hypothetically created columns were provided a nominal length of 650 mm, compressive-cylinder strength of concrete as 44 MPa, and steel yields strengths of 350 MPa and 365 MPa for inner and outer tubes, respectively. Among geometric parameters, ratio of diameter to thickness ratio for inner tube ($D_i/t_i = 24$ to 48) and outer tube ($D_0/t_0 = 45$ to 85) was varied in the generated 10-sets of numerical models. However, each generated column set had constant values for D_i/t_i and D_0/t_0 across the considered cross-sectional shapes. Confinement of concrete infill in each
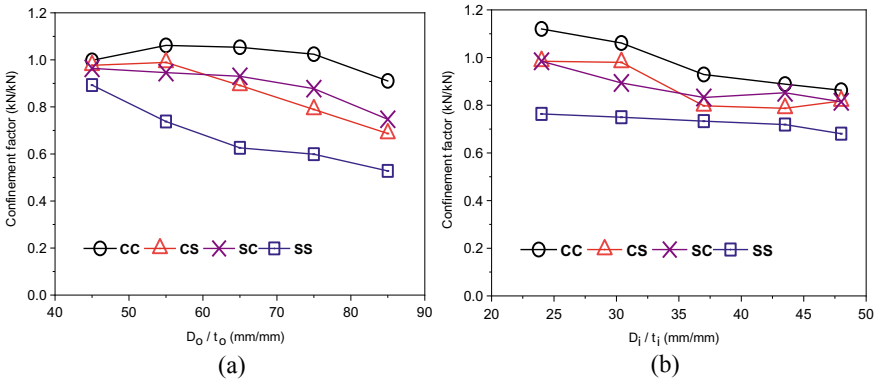
Fig. 5 Influence of steel tube slender ratios on confinement factor for multiple-shapes of CFDST columns: **a** outer steel tube; **b** inner steel tube; D_o = outer tube size; t_o = outer tube thickness; D_i = inner tube size; t_i = inner tube thickness

of the numerical models was measured by confinement factor. Confinement factor was defined as ratio of analytical ultimate axial load capacity ($P_{\text{ult.,NLFEA}}$) of CFDST column to its total summed capacity arrived from individual column components, i.e., inner tube ($f_{yi}.A_{si}$), outer tube ($f_{yo}.A_{s0}$), and concrete infill ($f_c'.A_c$) and is given by Eq. 8.

$$\text{Confinement factor (CF)} = \frac{P_{\text{ult.,NLFEA}}}{f_{yi}.A_{si} + f_{yo}.A_{s0} + f_c'.A_c} \qquad (8)$$

where f_{yi} and f_{y0} = yield stress of inner and outer steel tubes; A_{si}, A_{s0} and A_c = cross-sectional areas of inner tube, outer tube, and concrete infill, respectively.

Figure 5 shows the influence of diameter (or edge length)-to-thickness ratios of inner and outer steel tubes on confinement factor (CF). The inner and outer tube slenderness, i.e., D_0/t_0 and D_i/t_i have negative influence on concrete infill confinement. However, D_0/t_0 is clearly having more prominent negative effect on CF than D_i/t_i. Among considered CFDST column shapes, the decrease in CF is seen about 9% in CC, 30% in CS, 22% in SC, and 41% in SS when D_0/t_0 is varied from 45 to 85 by increasing D_0 (Fig. 5a). This indicates that increase in outer tube size (D_0) reduces concrete confinement in all column shapes with the most decrease in SS and the least in CC shape. Figure 5b shows that as D_i/t_i is increased from 24 to 48 by increasing D_i at constant D_0/t_0 ratio, CF decreases by about 23% in CC, 17% in CS and SC, and 11% in SS. Thus, increasing size of inner steel tube (D_i) reduces concrete confinement to greatest degree in CC and lowest in SS. Also Figs. 5a, b depict that among equivalent columns at any particular ratio of D_0/t_0 or D_i/t_i, CC provides highest CF, whereas SS shape develops the lowest CF. The other two column shapes, CS and SS have comparable CF values. The relative drop in CF in SS with respect to CC shape is about 11% at $D_0/t_0 = 45$, whereas this drop in concrete confinement

for SS increase to about 42% with increase in $D_0/t_0 = 85$ (Fig. 5a). However, this trend in relative drop for CF values of SS shape is reversed in Fig. 5b for equivalent columns. Such as for $D_i/t_i = 24$, drop in concrete confinement in SS with respect to CC shape is about 32% whereas same reduces to 21% at $D_i/t_i = 48$.

The influence of cross-sectional shape of CFDST columns with respect to CC on their ultimate axial load capacity ($P_{ult.}$) is shown in Fig. 6, and capacity values are summarized in Table 2. The average decrease in $P_{ult.}$ compared to CC is 12% in CS, 11% in SC, and 29% in SS (Fig. 6). This reduction in column capacities compared to CC can be attributed to the fact that ultimate axial load for each shape

Fig. 6 Ultimate axial load capacity of multiple-shape CFDST columns with respect to circle-circle (CC) shape
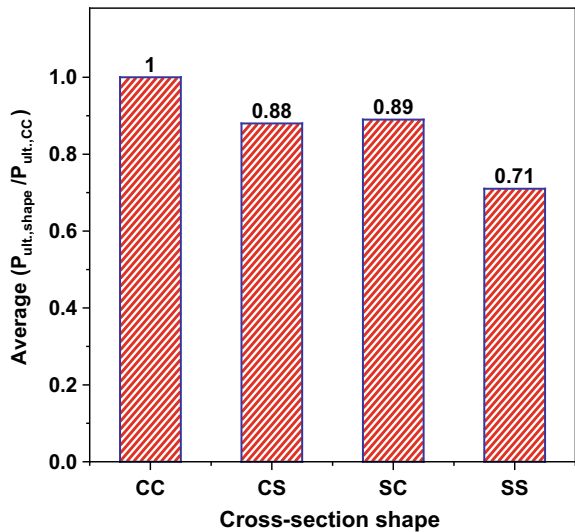
Table 2 Comparison of axial load capacities of equivalent multiple-shape CFDST columns

Column number	Ultimate axial load capacity: P_{ult} (kN)			
	CC	CS	SC	SS
1	2495	2325	2225	1736
2	4446	3355	3654	2580
3	1670	1635	1615	1495
4	3241	2743	2864	1928
5	4025	3102	3451	2356
6	2494	2303	2100	1762
7	2695	2369	2369	1837
8	2099	1802	1881	1656
9	1899	1683	1822	1537
10	1756	1664	1657	1384

has significant contribution from concrete fill confinement. Accordingly, a drop in confinement level is directly correlated to decease in $P_{ult.}$ for various column shapes. Such as average decrease in CF values compared to CC (recall, Fig. 5a, b) was 12% for CS, 11% SC, and 29% for SS, and these reductions in concrete confinement results in corresponding decrease in axial load capacities.

4 Summary and Conclusions

In the present study, nonlinear FE modeling methodology was used to reproduce the experimentally observed behavior of CFDST columns of multiple shapes (i.e., CC, CS, SC, and SS) under axial compression. The study utilized documented results of 40 CFDST columns (16 of CC shape and 8 each with CS, SC, and SS shapes) for successful validation of numerical models. The analytical models for all four shapes predicted axial compression behavior of CFDST columns in good agreement with experimental results. The degree of concrete confinement developed in each column shape including pre- and post-peak column behavior under axial compression was successfully captured by the analytical models and was validated against documented experimental results. The analytical values of ultimate axial load capacities of CFDST columns in all considered shapes were within 1–5% maximum errors compared to experimentally evaluated results.

A parametric study was performed on 40 additional CFDST numerical models (10 models each for CC, CS, SC, and SS shapes) to examine influence of cross-section shape on degree of concrete confinement produced and their ultimate axial load capacities. Analytical models were provided with equivalent cross-sectional areas for inner tube, outer tube, and concrete infill. The following conclusions can be drawn from this parametric study:

- CFDST column cross-sectional shape has a significant influence on degree of confinement produced for concrete infill, thereby directly affecting column behavior from elastic to ultimate states. Compared to CC shape, average decrease in confinement ratios was 12% for CS, 11% for SC, and 29% for SS for inner or outer tube slenderness ratio variations investigated in this study.
- The ultimate axial load capacity of the CFDST columns showed direct correlation with degree of concrete confinement produced on account of cross-sectional shape of the columns. Average decrease in ultimate column capacity compared to CC was 12% in CS, 11% in SC, and 29% in SS for CFDST columns with equivalent cross-sectional areas.
- Increase in diameter (or edge length)-to-thickness ratios, i.e., inner and outer tube slenderness has negative influence on concrete confinement in CFDST columns, with outer steel tube having more prominent effect than inner tube. The most decrease in confinement ratio (CF) was observed in SS (41%) and least in CC (9%) shapes for outer tube slenderness ratio variations. However, the maximum

decrease in CF is observed for CC (23%) and minimum for SS (11%) shapes when inner tube slenderness ratio is increased.

- CC shape showed highest confinement ratio and SS the lowest, whereas CS and SS showed comparable confinement for inner or outer tube slenderness ratio variations considered in this study.

Although, the study described herein was performed with rigorous NLFEA, the work was limited to only stub-column behavior. Additional comprehensive future studies are needed for more general understanding on influence of multiple cross-sectional shapes on concrete confinement and ultimate axial load capacities of slender CFDST columns.

References

1. Han LH, Li W, Bjorhovde R (2014) Developments and advanced applications of concrete filled steel tubular (CFST) structures: members. J Constr Steel Res 100:211–228
2. Liew JYR, Xiong MX, Xiong DX (2014) Design of high strength concrete filled tubular columns for tall buildings. J High-rise Build 3(3):215–221
3. Kitada T (1997) Ultimate strength and ductility of state-of-the-art concrete-filled steel bridge piers in Japan. Eng Struct 20(4–6):347–354
4. Chacón R, Mirambell E, Real E (2013) Strength and ductility of concrete-filled tubular piers of integral bridges. Eng Struct 46(1):234–246
5. Zakir M, Sofi FA, Naqash JA (2021) Experimentally verified behavior and confinement model for concrete in circular stiffened FRP-concrete-steel double-skin tubular columns. Structures 33:1144–1157, ISSN 2352-0124, https://doi.org/10.1016/j.istruc.2021.05.010
6. Zakir M, Sofi FA, Behera S (2021) Nonlinear finite element analysis of circular stiffened FRP-concrete-steel double-skin tubular columns (DSTCs) and experimental compressive behavior of multiple DSTC shapes. Structures 34:3283–3299, ISSN 2352-0124, https://doi.org/10.1016/j.istruc.2021.09.076
7. Wei S, Mau ST, Vipulanandan C, Mantrala SK (1995) Performance of new sandwich tube under axial loading: experiment. J Struct Eng 121(12):1806–1814
8. Tao Z, Han LH, Zhao XL (2004) Behaviour of concrete-filled double skin (CHS Inner and CHS Outer) steel tubular stub columns and beam-columns. J Constr Steel Res 60(8):1129–1158
9. Zhao XL, Grzebieta R, Elchalakani M (2002) Tests of concrete-filled double skin CHS composite stub columns. J Steel Compos Struct. 2(2):129–146
10. Uenaka K, Kitoh H, Sonoda K (2010) Concrete filled double skin circular stub columns under compression. Thin-Walled Struct. 48(1):19–24
11. Elchalakani M, Zhao XL, Grzebieta R (2002) Tests on concrete filled double-skin (CHS outer and SHS inner) composite short columns under axial compression. Thin Walled Struct 40(5):415–441
12. Zhao XL, Grzebieta R (2002) Strength and ductility of concrete filled double skin (SHS inner and SHS outer) tubes. Thin-Walled Struct. 40(2):199–213
13. Han LH, Tao Z, Huang H, Zhao XL (2004) Concrete-filled double-skin (SHS outer and CHS inner) steel tubular beam-columns. Thin-Walled Struct. 42(9):1329–1355
14. Wan CY, Zha XX (2016) Nonlinear analysis and design of concrete-filled dual steel tubular columns under axial loading. Steel Compos Struct 20(3):571–597
15. Xiong MX, Xiong DX, Liew JYR (2017) Axial performance of short concrete filled steel tubes with high-and ultra-high-strength materials. Eng Struct 136(4):494–510
16. Ibañez C, Romero ML, Espinos A, Portolés J, Albero V (2017) Ultra-high strength concrete on eccentrically loaded slender circular concrete-filled dual steel columns. Structures 12:64–74

17. Wang F, Young B, Gardner L (2019) Compressive testing and numerical modelling of concrete filled double skin CHS with austenitic stainless-steel outer tubes. Thin-Walled Struct. 141:345–359

18. Huang H, Han LH, Tao Z, Zhao XL (2010) Analytical behaviour of concrete-filled double skin steel tubular (CFDST) stub columns. J Constr Steel Res 66(4):542–555

19. Tao Z, Wang ZB, Yu Q (2013) Finite element modelling of concrete-filled steel stub columns under axial compression. J Constr Steel Res 89:121–131

20. Pagoulatou M, Sheehan T, Dai XH, Lam D (2014) Finite element analysis on the capacity of circular concrete-filled double-skin steel tubular (CFDST) stub columns. Eng Struct 72:102–112

21. Hassanein MF, Kharoob OF, Gardner L (2015) Behaviour and design of square concrete-filled double Skin tubular columns with inner circular Tubes. Eng Struct 100:410–424

22. Hassanein MF, Elchalakani M, Karrech A, Patel VI, Yang B (2018) Behaviour of concrete-filled double-skin short columns under compression through finite element modelling: SHS outer and SHS inner tubes. Structures 14:358–375

23. Hassanein MF, Elchalakani M, Karrech A, Patel VI, Daher E (2018) Finite element modelling of concrete-filled double-skin short compression members with CHS outer and SHS inner tubes. Mar Struct 61:85–99

24. Hassanein MF, Patel VI, Elchalakani M, Thai H-T (2018) Finite element analysis of large diameter high strength octagonal CFST short columns. Thin-Walled Struct 123:467–482

25. Wang FC, Han LH, Li W (2018) Analytical behaviour of CFDST stub columns with external stainless-steel tubes under axial compression. Thin-Walled Struct. 127:756–768

26. Liang QQ (2018) Numerical simulation of high strength circular double-skin concrete-filled steel tubular slender columns. Eng Struct 168:205–217

27. Ayough P, Sulong NHR, Ibrahim Z, Hsiao PC (2020) Nonlinear analysis of square concrete-filled double skin steel tubular columns under axial compression. Eng Struct 216:1–18

28. ANSYS, Release, 19.0.: [Computer software]. ANSYS Inc, Canonsburg, USA (2019)

29. Sofi FA, Steelman JS (2017) Parametric influence of bearing restraint on nonlinear flexural behaviour and ultimate capacity of steel girder bridges. J Bridge Eng 22(7):1–18

30. Sofi FA, Steelman JS (2019) Nonlinear flexural distribution behaviour and ultimate system capacity of skewed steel girder bridges. Eng Struct 197:1–19

31. Sofi FA, Steelman JS (2021) Using committees of artificial neural networks with finite element modeling for steel girder bridge load rating estimation. Structures 33:533–553, ISSN 2352-0124, https://doi.org/10.1016/j.istruc.2021.04.056

32. Sofi FA (2017) Structural System-Based Evaluation of Steel Girder Highway Bridges and Artificial Neural Network (ANN) Implementation for Bridge Asset Management. Doctoral Dissertation, University of Nebraska-Lincoln. https://doi.org/ETD collection for University of Nebraska - Lincoln. AAI10682985

33. Bazant ZP, Gambarova PG (1984) Crack shear in concrete: crack band microplane model. J Struct Eng 110(9):2015–2035

34. Zhao X, Han B, Grzebieta R (2002) Plastic mechanism analysis of concrete-filled double skin (SHS inner and SHS outer) stub columns. Thin-Walled Struct. 40(10):815–833

35. ACI 318–399 (1999) Building code requirements for structural concrete and commentary. American Concrete Institute, Detroit, USA

36. Popovics S (1973) A numerical approach to the complete stress-strain curves for concrete. Cement and Concr. Res. 3(5):583–599

37. Mander JB, Priestley MJN, Park R (1988) Theoretical stress–strain model for confined concrete. J Struct Eng 114(8):1804–1826

38. Tomii M, Sakino K (1979) Elastic–plastic behavior of concrete filled square steel tubular beam-columns. Trans Archit Inst Jpn. 280:111–120

39. Han LH, Huo JS (2003) Concrete-filled HSS columns after exposure to ISO-834 standard fire. J Struct Eng 129(1):68–78